RESEARCH ARTICLE | AUGUST 01 2024

A particle-in-cell study of electrostatic potential well formation in an edge-confined non-neutral plasma

W. Hongtrakul; C. A. Ordonez ; D. L. Weathers

AIP Advances 14, 085105 (2024)
https://doi.org/10.1063/5.0219656

A particle-in-cell study of electrostatic potential well formation in an edge-confined non-neutral plasma

Cite as: AIP Advances 14, 085105 (2024); doi: 10.1063/5.0219656
Submitted: 18 May 2024 • Accepted: 16 July 2024 •
Published Online: 1 August 2024

W. Hongtrakul, C. A. Ordonez, and D. L. Weathers[a)]

AFFILIATIONS

Department of Physics, University of North Texas, Denton, Texas 76203, USA

[a)]Author to whom correspondence should be addressed: duncan.weathers@unt.edu

ABSTRACT

An edge-confined single-species plasma will relax to create a potential energy hill that climbs from the boundary. This hill represents a potential well for species of the opposite sign and can be a means to confine the second species. With this ultimate application in mind, we have studied the relation between the plasma temperature, the number of confined particles, and the electrostatic potential well that forms in a fully non-neutral plasma of electrons in a trapping volume with an artificially structured boundary (ASB). An ASB is a structure that produces periodic short-range static electric and magnetic fields for confining a plasma. To perform a detailed analysis on this topic, simulations using a particle-in-cell code have been performed. By varying the configurational elements of the ASB, such as the bias on the boundary electrodes and the internal radius of the structure, coupled with a course thermalization process and a prescribed threshold for particle leakage, potential well values were determined for a range of plasma temperatures and confinement conditions. Maximum well depths were observed below a threshold plasma temperature in each configuration. This study gives insight into the limitations of primary particle confinement with this type of structure and optimal conditions for the formation of a potential well that might be utilized to confine a second species.

I. INTRODUCTION

Traps for non-neutral plasmas have been utilized since the 20th century for a wide range of applications. These include, for example, the confinement of two-species plasma for recombination studies,[1,2] production and storage of particles and anti-particles,[3] generation of particle beams,[4] confinement of hot plasma for thermonuclear fusion power,[5–7] and other experiments in atomic and molecular physics.[8] Most traps use strong, pervasive magnetic fields to confine the plasma, which can cause heating effects and also leaves no region with weak or no fields in the trapping volume. However, for some applications, it may be desirable for a trap to provide both good confinement and a large weak-field or field-free region in which the particles can reside. One such design is a trap that utilizes an artificially structured boundary (ASB) in the form of a "linear array of magnetic field ring cusps"[9] created from a series of periodic magnetic fields which, when superimposed, result in strong fields near the boundary that tend to cancel out at distances further away from the boundary.

One prime example that uses this type of confinement is the Jupiter-2M trap along with its variations.[10–12] This trap uses a series of magnetic coils with pulsed opposing currents in adjacent coils to generate the type of magnetic fields mentioned above.

Another prototypical ASB trap, which will be the main focus of this paper, is constructed from a series of magnetized rare-earth permanent ring magnets aligned axially with the magnetic poles in a north–north south–south configuration. This alignment creates a series of magnetic field cusps that are short in range and can reflect charged particles of either sign at grazing angles of incidence.[13,14] Particles with a normal angle of incidence may pass through the cusps but can be stopped with electrostatic plugging by applying electric fields.[15] The most straightforward electrostatic plugging scheme will reflect only one sign of charged particles. However, Pacheco *et al.* performed self-consistent finite-difference

calculations to show that an idealized edge-confined non-neutral plasma in a steady-state (dynamic equilibrium) situation will distribute itself to produce a potential well suitable for confining particles of the opposite charge.[16] Hedlof and Ordonez performed more realistic particle-in-cell simulations of a non-neutral plasma in a full ASB trap to demonstrate the formation of this type of potential well under non-equilibrium conditions,[17] and Kiester *et al.* used a particle-in-cell simulation to show the formation of a potential well in a tenuous electron plasma in a leaky trap and experimentally corroborated the confinement of hydrogen ions in this well.[18] In what follows, we report on a computational study of potential wells of this type formed by fully non-neutral electron plasmas confined by an ASB trap based on the design of the device built by Kiester *et al.* The well formation has been studied as a function of plasma temperature and for a range of boundary conditions to establish the corresponding well parameters and conditions for well formation that could be optimized to confine a second species.

The following sections will explain the simulation code and simulation model that were used, the simulation procedures, how we have introduced a thermalization process, and how we calculated the leak rate for an accurate comparison between simulations, as well as finally show a discussion about the results.

II. SIMULATION MODEL

In order to perform a detailed analysis of the plasma in an ASB trap, we employed the simulation code XOOPIC (X11-based Object Oriented Particle in Cell)[19] that runs on desktop computers. XOOPIC is a particle-in-cell with Monte-Carlo-collision (PIC-MCC) code[20] that allows the simulation of physical systems that can include plasmas, beams of charged particles, externally generated electric and magnetic fields, and low- to moderate-density neutral gases with a wide variety of boundary conditions.

Whereas the electric fields in the simulation were generated using XOOPIC built in an electrostatic solver, the magnetic fields were generated using RADIA.[21] RADIA is a quasi-analytic code that uses the analytical magnetic field solution of magnetized polyhedron segments to approximate the solution of more complex magnet geometries.

In order to minimize the simulation time and be able to obtain data for many different simulation configurations, we chose to simulate a short section of a cylindrical ASB structure (Fig. 1). The middle section of the simulation should also be representative of the middle of a long trap as any electrostatic effects from beyond the axial ends of the small simulation volume that would be seen in a longer trap only contribute marginally to the mid-plane radial fields. Simulations of ASB sections that were 50% longer in axial length yielded very similar results to those of the short ASB section simulations for the size of the well depth and the plasma temperature in each area of the middle of the simulation. Therefore, we focus on using these smaller-sized simulations moving forward.

Three sets of simulations have been performed in total, denoted as small-radius low-bias simulations, small-radius high-bias simulations, and large-radius low-bias simulations. The small-radius simulations are based on a real trap that was previously constructed and is described elsewhere.[18]

The small-radius simulations were carried out using a cylindrically symmetric two-dimensional grid with 196 grid spaces axially and 640 grid spaces radially. The total spatial grid size was 24.5 mm axially by 16 mm radially, and simulations were conducted with time steps of 5×10^{-13} s.

The simulation model consisted of four annular magnets having fields consistent with those of axially magnetized NdFeB n42-grade magnets, each with a thickness of 3.125 mm, an internal radius of 9.525 mm, an outer radius of 16 mm, and a residual magnetization of 1.28 T. The magnets alternated with three annular plugging electrodes of a thickness of 2.00 mm and internal radius of 11.11 mm and with two plugging electrodes of half this thickness, one at each end of the simulated segment. Adjacent magnets and electrodes were separated by a 0.5 mm gap. The magnets were aligned such that like magnetic poles faced each other in a north–north south–south configuration.

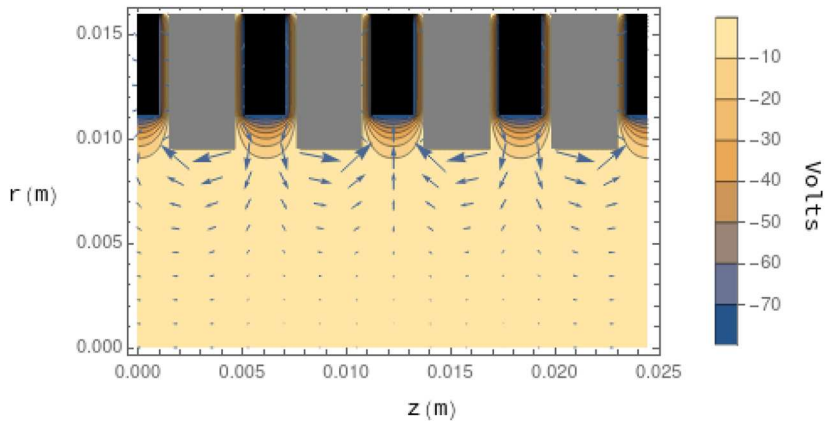

FIG. 1. Radial section of the cylindrically symmetric small-radius trap geometry. The large and small rectangles at the top of the figure represent the magnets and plugging electrodes, respectively. The magnetic field (arrows) and equipotential contours for the low-bias case with no particles present are shown.

While the top wall of the simulation ($0 \le z \le 24.5$ mm, $r = 16$ mm) and magnets were grounded (0 V), both the left-side wall ($z = 0$ mm, $0 \le r \le 16$ mm) and the right-side wall ($z = 24.5$ mm, $0 \le r \le 16$ mm) were set to reflect any particles that crossed them back into the simulation environment. Any particles that crossed the cylindrical axis ($0 \le z \le 24.5$ mm, $r = 0$ mm) were also mirrored back into the simulated environment, so particles could only be lost when they touched the magnets or electrodes. Dirichlet boundary conditions were applied at the top wall and at the surfaces of the magnets and electrodes, and Neumann boundary conditions were applied at the left-side and right-side walls and the cylindrical axis.

The difference between the first two sets of simulations was the bias on the electrodes. The first set, the small-radius low-bias simulations, had electrodes biased at −80 V, while the second set, the small-radius high-bias simulations, had electrodes biased at −240 V. These were chosen to give a good comparison between a low-bias confinement and a high-bias confinement, with voltages that should be easily obtainable in experiments.

The simulations with a large radius had mostly the same settings and same dimensions for the magnets and electrodes as the first two sets of simulations, except the internal radius of the simulated magnets was doubled to 19.05 mm, the outer radius of the magnets was increased to 25.525 mm, and the internal radius of the electrodes was increased to 20.635 mm. The grid of these simulations was also changed to have 1021 grid spaces radially, corresponding to a total spatial size of 25.525 mm, while the axial grid spacing remained the same. The simulation parameters are summarized in Table I.

Figure 1 shows the magnetic field along with the equipotential contours of the small-radius simulations with no particles present; the fields were similar for the large-radius simulations. In both cases, the electric potential was ~zero except near the electrodes. In the small-radius simulations, the magnetic fields near the magnets ($r \sim 0.009$ m) were on the order of 10^{-1} T, while the magnetic fields along the axis ($r \sim 0$ m) were on the order of 10^{-2} T and smaller. For the large-radius simulations, the magnetic fields near the magnets ($r \sim 0.018$ m) were also on the order of 10^{-1} T, while the magnetic fields along the axis ($r \sim 0$ m) were on the order of 10^{-3} T and smaller.

TABLE I. Simulation parameters.

Parameter	Value	
Simulation overall axial length	24.5 mm	
Simulation overall radius	16 mm (sm.)	25.525 mm (lg.)
Magnet inner radius	9.525 mm (sm.)	19.05 mm (lg.)
Electrode inner radius	11.11 mm (sm.)	20.635 mm (lg.)
Magnet/electrode outer radius	16 mm (sm.)	25.525 (lg.)
Magnet thickness	3.125 mm	
Electrode thickness	2 mm (full)	1 mm (half)
Magnet–electrode spacing	0.5 mm	
Magnet residual magnetization	1.28 T	
Magnet electrical potential	0 V	
Electrode potential	−80 V (low)	−240 V (high)
Grid size (axial × radial)	196 × 640 (sm.)	196 × 1021 (lg.)
Time step	5×10^{-13} s	

III. SIMULATION PROCEDURES

At the beginning of all but the lowest-temperature simulations (discussed below), a uniform spatial distribution of electrons was loaded directly into essentially all the simulation volume except for that occupied by the magnets and electrodes. This was done to maximize the amount of charge ultimately remaining in the trap in order to obtain the maximum size of the potential well that can be formed.

Each simulation started with the same number of virtual particles: 400 000 for the small-radius simulations and, to help reduce the simulation time, 200 000 for the large-radius simulations. However, each simulation was started with a different initial plasma temperature and a different real-to-virtual particle ratio—based on an informed guess—which was then adjusted until each simulation reached the same particle leak rate (explained in Sec. III B). The real-to-virtual particle ratios used in these simulations ranged from 75 to 8700.

Each simulation was run for 27–30 ns of simulation time from inception before being put through a thermalization process (explained in Sec. III A) and then run again for another 27–30 ns of simulation time. This process was repeated one more time, resulting in two thermalization steps for each simulation before data were collected and analyzed. If the particle leak rate at the end of the final step did not match the target, then the real-to-virtual particle ratio

TABLE II. Numerical data for the small-radius low-bias simulations.

Initial T (eV)	Final T (eV)	No. of real particles	Well depth (V)
3.33[a]	5.07	1 827 287 595	25.26
0	6.38	1 122 004 800	25.40
3.33	7.15	890 975 100	24.79
6.67	8.31	619 781 625	20.86
10	10.07	271 778 925	10.39
12	11.9	25 676 025	0.73

[a]Non-uniform initial spatial distribution.

TABLE III. Numerical data for the small-radius high-bias simulations.

Initial KE (eV)	Final T (eV)	No. of real particles	Well depth (V)
6.67[a]	10.06	3 933 485 760	50.33
10[a]	11.43	3 247 485 540	50.37
0	13.25	2 600 821 500	51.52
3.33	13.77	2 295 180 000	52
6.67	14.55	1 963 564 200	49.01
10	15.62	1 765 209 600	44.90
13.33	17.49	1 357 100 250	41.21
16.67	19.77	1 188 306 000	39.10
20	22.09	995 910 000	34.77
23.33	24.53	661 718 850	23.88
30	30.23	231 414 300	8.74
36.67	35.32	101 255 100	2.99

[a]Non-uniform initial spatial distribution.

TABLE IV. Numerical data for the large-radius low-bias simulations.

Initial KE (eV)	Final T (eV)	No. of real particles	Well depth (V)
3.33[a]	6.11	2 251 348 155	41.30
0	7.58	1 600 149 600	42.64
3.33	8.19	1 151 152 200	36.69
6.67	9.07	832 136 100	30.39
10	10.6	490 141 800	20.45
13.33	13.05	136 984 500	6.22

[a]Non-uniform initial spatial distribution.

at the beginning of the first step was adjusted and the entire process was repeated.

It should be mentioned that, even though changing the real-to-virtual particle ratio for a fixed total charge resulted in different levels of random noise in the resulting final electron density data, tests showed that the values of the well depth and leak rate were still practically the same for simulations that had the same initial conditions otherwise. Therefore, results presented below should consistently represent the number of particles and well depth for each corresponding plasma temperature.

Simulations as described above that started with 0 eV electrons ended with a non-zero plasma temperature because of the initial potential energy of the charge configuration. In order to reach lower final plasma temperatures, simulations were loaded initially with a non-uniform electron distribution with lower potential energy than the uniform distribution. The initial distribution used in these cases was the final electron distribution from the simulation that started with uniformly distributed 0 eV electrons. The plasma temperature of this loaded distribution was then lowered before starting the new simulation, and the electron density was once again adjusted in multiple iterations until the simulation reached the required leak rate after going through one more thermalization step. Simulations for which this process was followed are noted in Tables II–IV.

A. Introducing thermalization

One limitation of XOOPIC, and of particle-in-cell codes in general, is the inability to simulate direct microscopic energy transfer from one charged particle to another, resulting in an inability to reach thermal equilibrium quickly. One approach to overcoming this difficulty was developed and applied by Gomberoff *et al.*,[22–24] in which computational local thermal equilibrium for a complex trapping geometry is attained through a multi-stage process. This process begins with a known, coarse, idealized particle distribution for a simpler geometry, with a gradual computational refinement first to reach a more realistic equilibrium, and then to introduce a more complex geometry. In the present study, we have taken a different approach by introducing a thermalization process in which, after every 27–30 ns of simulation time, the density distribution of the electrons was saved and then reloaded after imposing a uniform thermal energy distribution on the electron plasma with temperature T corresponding to the average kinetic energy ⟨K⟩ of the electrons in the just-ended simulation step. To obtain this thermal distribution, each electron's initial velocity components were sampled from a Maxwellian velocity distribution associated with a temperature T = (2/3) ⟨K⟩ in energy units. Performing two thermalization steps per simulation proved to make every area of the simulation volume have approximately the same final temperature. It also allowed the electrons to move a short distance across the magnetic field by virtue of the bin size used to save the distribution. Although performing more than two thermalization steps per simulation resulted in small further changes in the resulting electron distribution, using just two thermalization steps was considered sufficient to capture the essential behavior of the system.

B. Leak rate calculations

To have a good comparison of the particle densities and electric potential distributions at different plasma temperatures, we have compared the data after adjusting each simulation to have roughly the same relative particle leak rate. In order to calculate the leak rate, the number of particles vs time after the last thermalization step of each simulation was fitted with a function of the form $\ln\left(Ae^{-Bt} + Ce^{-Dt}\right)$, as shown in Fig. 2. Behavior similar to that seen in the figure was found in all the simulations: particles were initially lost at a rapid, approximately linear rate (with slope –B), which gave way after the first few nanoseconds to a slower, more sustained loss rate that was also approximately linear over the timescale of the simulation (with slope –D). The initial, rapid loss was dominated by particles starting the simulation step on unconfined trajectories along magnetic field lines that carried them past the electrode corners into adjacent magnet faces. These were particles that had ended the previous simulation step on confined trajectories, but that had been shifted across the magnetic field during the thermalization process by virtue of the finite bin size used. The slower, more sustained loss was dominated by particles that started the simulation step on confined trajectories, but that were subsequently pushed by interactions with the rest of the plasma into the same magnetic field region that had carried the first group of particles out of the simulation. These unconfined trajectories lay just inside the arched boundaries separating the occupied from unoccupied regions around the magnet edges seen in Fig. 4.

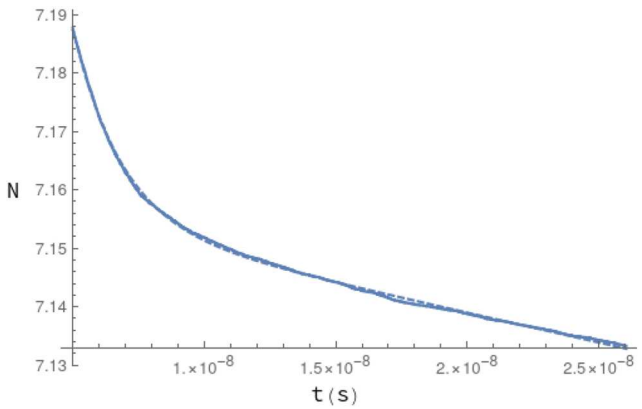

FIG. 2. Example of scaled number of particles vs time during the final step of a simulation. The solid line represents the simulation data and the dashed line represents the model curve fit.

The slower leak rate characterized by the D fitting parameter was used to compare the various simulations. To facilitate fitting and comparing the number of particles vs time for each simulation, the number of virtual particles at the end of each small-radius simulation was scaled down by a factor of 50 000; this is reflected in the vertical scale shown in Fig. 2. Similarly, for the large-radius simulations, the number of virtual particles at the end of each simulation was scaled down by a factor of 25 000. For these scaled data, we chose a D value of $1 \times 10^6 \pm 70\,000\ s^{-1}$ as the target for each simulation. Therefore, the electron number was adjusted by changing the real-to-virtual particle ratio, and each simulation was repeated until it exhibited a D parameter in this range. If we assume that the slower, approximately linear particle leak rate over the timescale of each simulation was actually part of a decaying exponential, then the target D value corresponds to a trapping lifetime of 1 μs.

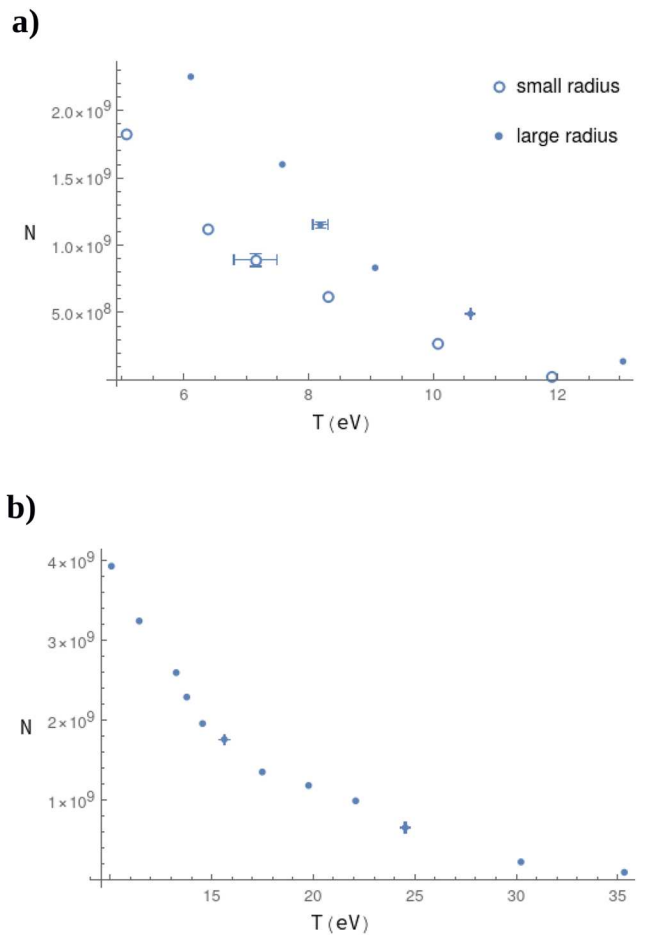

FIG. 3. (a) Final number of particles vs temperature for the large-radius low-bias and small-radius low-bias simulations. The open circles represent the small-radius low-bias simulations and the small solid dots represent the large-radius low-bias simulations. (b) Final number of particles vs temperature for the small-radius high-bias simulation. Estimated uncertainties are shown for select plotted values.

IV. RESULTS AND DISCUSSION

All the simulated trap configurations were found to confine non-neutral electron populations, which in turn distributed themselves to form potential wells in the trap interiors. In each configuration, the number of trapped electrons was found to decrease monotonically with increasing plasma temperature, as shown in

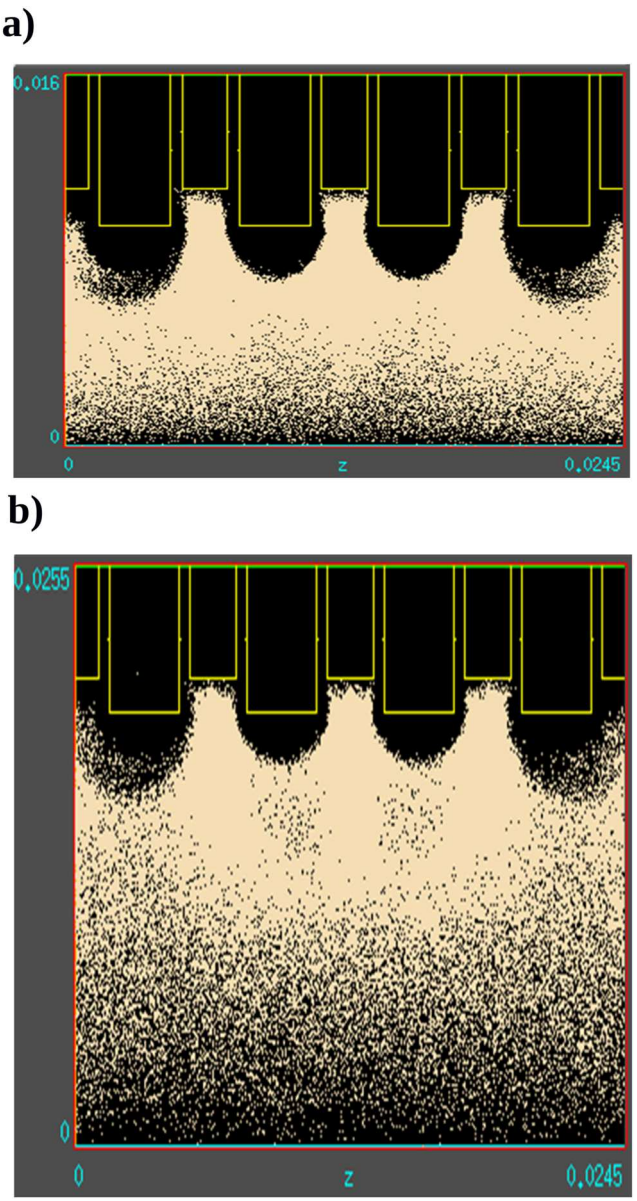

FIG. 4. The cylindrical projection of the spatial distribution of electrons from the end of (a) a small-radius simulation (6.38 eV electron temperature) and (b) a large-radius simulation (7.58 eV electron temperature). Electrons are represented by white dots, and outlines of the magnets and electrodes are shown. Both axes are in m.

Fig. 3. The overall number of confined electrons at a given temperature was seen to increase with increasing plugging electrode potential. In the small-radius simulations, the temperature corresponding to a particular number of confined electrons scaled very closely with the electrode potential. This is consistent with the magnetic confinement being similar in the low- and high-bias cases, to be expected because of the small Larmor radii in the magnetic cusps, which were generally no more than a few tens of micrometers. The number of confined electrons was also seen to increase with the radial size of the trap; at a given temperature, the number of confined electrons increased by a factor typically slightly less than two when the internal radius of the trap was doubled. This scaling reflects the amount of charge necessary to produce electric fields of the same magnitude outside different-sized quasi-cylindrical charge distributions.

The final distributions of confined electrons were nonuniform, with both shape and size dependent on the plasma temperature. Figure 4 shows the cylindrical projection of the spatial distribution of electrons at the end of representative small-radius and large-radius simulations. The distribution of confined electrons along the magnetic field near the outer trap boundary is apparent. Furthermore, one can see the proximity of the electron distributions to the plugging electrodes, which is where particle leakage was likely to occur after longer simulation times. The overall thinning of the electron distribution toward the radial center of the trap is also evident in Fig. 4. Near the magnets and electrodes in particular, the electron distribution can be seen to vary with the axial position. In the remainder of this discussion, radial particle distributions and potentials in the mid-plane (z = 0.012 25 m) of each simulated trap are considered primarily, but this mid-cusp profile captures the features important to particle confinement and potential well formation.

Figure 5 shows the number densities of electrons in the mid-plane of the small-radius, low-bias simulation for different plasma temperatures. Again, each of these curves is for a fully-loaded trap at the given plasma temperature with the prescribed particle leakage rate. Similar distributions were found for the other sets of

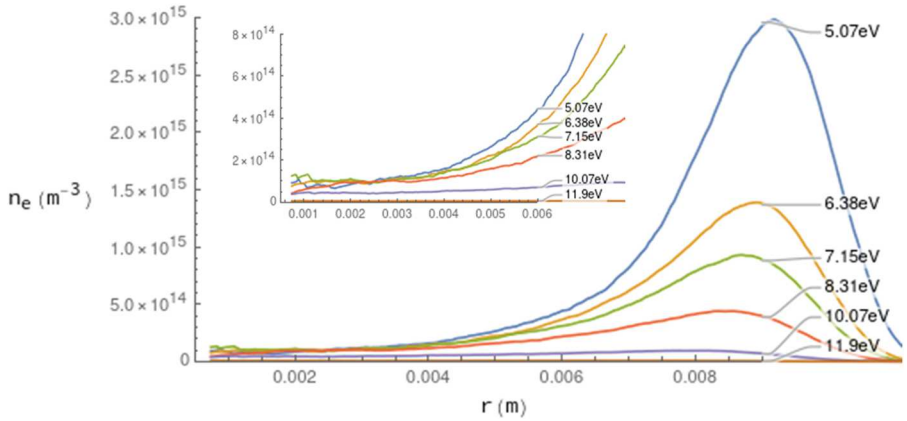

FIG. 5. The average number density of electrons in the middle of the simulation volume (z = 0.012 25 m) of the small-radius low-bias simulations. The inset shows a zoomed-in view of the densities at small r. Each curve is labeled with the associated plasma temperature in energy units.

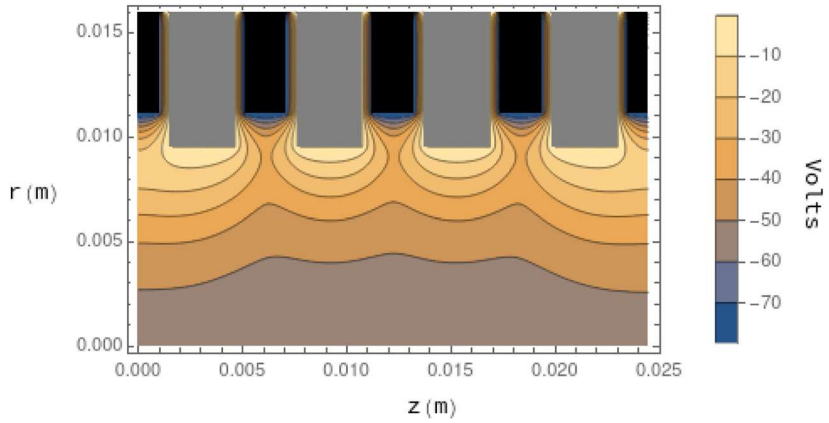

FIG. 6. Equipotential contour plot for the small-radius low-bias simulation with particles filled up to the prescribed leak rate and with maximum well depth (6.38 eV electron temperature).

simulations. The areas under the curves shown in Fig. 5 correspond approximately to the associated total numbers of trapped particles shown in Fig. 3(a). The general shape of each distribution is peaked near the outer radius of the trap, falling off toward smaller radii and even more rapidly toward larger radii. At the lowest temperature, the peak electron density is $n_e \approx 3 \times 10^{15}$ m^{-3} with corresponding Debye length $\lambda_D \approx 3 \times 10^{-4}$ m; these values at the center of the trap are $n_e \approx 1 \times 10^{14}$ m^{-3} and $\lambda_D \approx 1.7 \times 10^{-3}$ m (~0.2 trap radii). The peak electron density is ~30 times the density at the center of the trap at this temperature; this ratio decreases with increasing temperature until at the highest temperature, the density becomes approximately uniform. Interestingly, the densities at the center of the trap are within a factor of two of each other for all but the highest temperatures. The Debye length becomes more uniform with increasing temperature, reaching $\lambda_D \approx 1.1 \times 10^{-2}$ m for most radii at the highest temperature. For the small-radius, high-bias simulations, the low temperature electron densities and Debye lengths were all ~1.5 times the corresponding values mentioned above. For the large-radius, low-bias simulation at the lowest temperature, the peak electron density was $n_e \approx 1.4 \times 10^{15}$ m^{-3} ($\lambda_D \approx 6 \times 10^{-4}$ m)

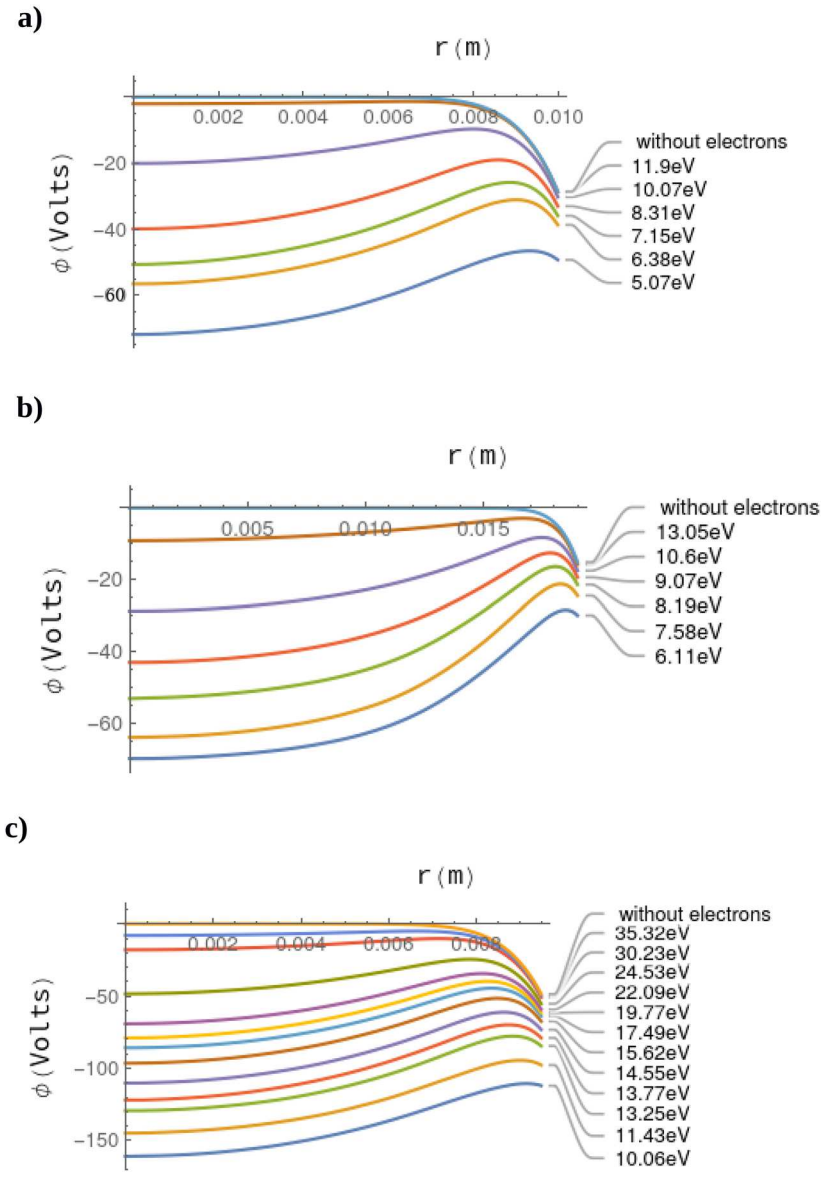

FIG. 7. The electric potential Φ in the mid-plane of the simulation volume (z = 0.012 25 m) of (a) small-radius low-bias simulations (b) large-radius low-bias simulations and (c) small-radius high-bias simulations. Each curve is labeled with the associated plasma temperature in energy units.

while at the center of the trap, $n_e \approx 2 \times 10^{13}$ m^{-3} ($\lambda_D \approx 5 \times 10^{-3}$ m). For both these sets of simulations, at the highest temperatures, the Debye length approached the same value as for the small-radius, low-bias case. In all simulations, the proportion of electrons at large radii increased dramatically with decreasing temperature; the position of the distribution peak shifted slightly to larger radii as well. All of this is consistent with the competition between mutual electrostatic repulsion pushing electrons outward and thermal energy allowing electron incursion inward against this repulsion. Note that the characteristic length scales over which the electron density distribution decreases inward toward smaller radii from the peak, as seen in Fig. 5, are of the same order as the corresponding Debye lengths.

Figure 6 shows an equipotential contour plot for a small-radius low-bias simulation fully loaded with electrons. The contours are convoluted near the outer trap boundary, wrapping around the magnet edges and into the cusp regions, but become much smoother closer to the axis. Inside a radius of ~0.005 m in this case, the radial

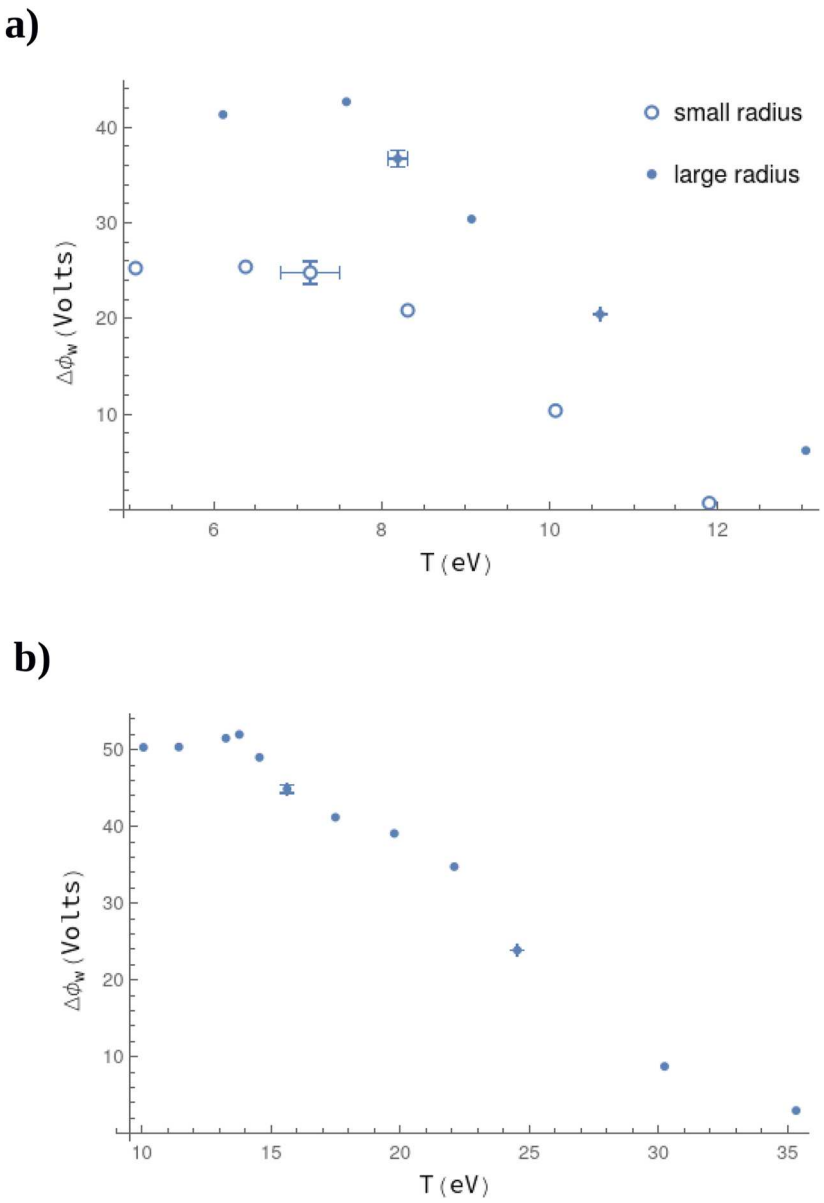

FIG. 8. (a) Well depth $\Delta\Phi_w$ vs temperature for the large-radius low-bias and small-radius low-bias simulations. The open circles represent the small-radius low-bias simulations and the small solid dots represent the large-radius low-bias simulations. (b) Well depth $\Delta\Phi_w$ vs temperature of the small-radius high-bias simulations. Estimated uncertainties are shown for select plotted values.

potential profile becomes nearly uniform for axial positions in the interior half of the trap between z ~ 0.006 m and z ~ 0.018 m.

The electric potential in the mid-plane of each simulation configuration is shown for different plasma temperatures in Fig. 7. The negative-going potential well that forms in the center of the trap is plainly evident. With no electrons in the trap, the mid-plane potential increases from the negative value Φ_0 at the plugging electrode to zero in the interior of the trap. As the number of confined electrons increases, their negative charge causes the overall electric potential in the interior of the trap to decrease from zero. Because the confined electrons are distributed throughout the interior of the trap, the potential due to this charge decreases as one moves radially inward through the distribution, which is the ultimate origin of the potential well. The combination of these two oppositely changing contributions—the potential due to the confined charge and the potential from the boundary electrode—produces a maximum Φ_{max} in the potential near the outer radial trap boundary. The ratio of the potential difference $\Delta\Phi = \Phi_{max} - \Phi_0$ to the temperature T is closely related to the leak rate of electrons as it determines the density of electrons at the electrode relative to the density at the peak of the distribution according to $n/n_{max} = \exp(q\Delta\Phi/T)$, where q is the electron charge. As more electrons are added to the trap at a given temperature, Φ_{max} becomes more negative, increasing this ratio and increasing the relative leak rate. For both of the low-bias simulations, the $q\Delta\Phi/T$ ratio was ~7 for the electron densities that produced the prescribed leakage rate; for the high bias simulation, this ratio ranged between ~7 and 12.

The depth of the potential well $\Delta\Phi_W = \Phi_{max} - \Phi_{axis}$ in the fully-loaded trap depends on the plasma temperature and the corresponding density distribution for given boundary conditions, as shown in Fig. 8 and presented in Tables II–IV. At the highest temperatures and lowest electron densities, the amount of charge in the trap, although relatively uniformly distributed, is small and produces a very shallow well. As the plasma temperature decreases, the electron distribution grows and more charge is confined. At first, these changes decrease the electric potential at the center of the trap faster than near the edge and the well deepens, but as proportionately more charge is added at larger radii, the shape of the part of the potential due to the charge in the trap flattens near the axis and becomes steeper—i.e., it reflects a larger radial electric field due to the charge—towards the outer radial trap edge. This field is countered by the opposing electric field from the plugging electrode, and the maxima in the electric potential and charge density occur at the radius where these fields balance. This balance point is pushed outward with the addition of charge, and both contributions to the potential—from the charge distribution and the electrode—decrease at the balance point as it moves outward. Thus, the maximum in the overall potential Φ_{max} decreases, and at some point, its rate of decrease matches the rate at which the potential at the center of the trap decreases. The depth of the potential well then no longer increases with further decreases in plasma temperature, despite the corresponding increase in confined charge. Although not explored here, one might predict that with further decreases in plasma temperature, the potential at the trap center would eventually approach its floor—the plugging electrode potential—while Φ_{max} would continue to decrease, causing $\Delta\Phi_W$ to decrease back toward zero.

The uncertainties presented in Figs. 3 and 8 were determined by collecting data at slightly different times during the last thermalization step and using different random number seeds for selected simulations. The maximum differences found in the results are represented by the lengths of the error bars. It is seen that the results at high plasma temperatures tend to have less uncertainty than the results at lower temperatures.

Comparing the different simulation cases, the small-radius low-bias configuration produced a maximum well depth of ~25 V, or ~30% of the plugging electrode potential, for plasma temperatures less than ~7 eV. For the small-radius high-bias configuration, a maximum well depth of ~50 V was obtained for plasma temperatures below ~14 eV. Hence, these two metrics for the well doubled compared to the first case, although the plugging potential was tripled. The well shapes for these two cases were very similar. In the large-radius low-bias configuration, the larger size allowed for more charge to be confined than the first case for the same plasma temperature scales, so the maximum well depth increased to ~42 V, or slightly over 50% of the plugging electrode potential, for plasma temperatures less than ~8 eV. Other than being larger in radius, the well shape in this case was flatter near its center than the other two cases. Finally, the largest plasma temperatures that could be confined according to the prescribed leakage criterion were about 0.15 $e\Phi_0$ in the first two cases and slightly higher in the third.

V. CONCLUSIONS

We have simulated non-neutral electron plasma confinement by a cylindrical ASB trap under different realistic boundary configurations, employing a course plasma thermalization technique to hasten the approach to equilibrium, and have determined maximal trap loading conditions as a function of plasma temperature subject to a prescribed particle leakage rate. By examining electron distributions and electrostatic potential in a representative section of the trap, we have observed the formation of an electrostatic potential well in the electron plasma and have gained insight into the factors that influence it. We have found that the well depth increases with decreasing plasma temperature to a point, beyond which the well depth remains essentially constant even with further increases in confined charge in the studied range. In addition, both larger trapping volume and higher surface potential at the boundary were found to increase the number of confined particles and the size of the potential well. The well depth reached as high as 50% of the value of the boundary electrode potential under the conditions of our study. A next step would be to introduce positive plasma species to study the effectiveness of the electron potential well at confining the second species and optimal conditions for that confinement.

ACKNOWLEDGMENTS

This material is based upon the work supported by the National Science Foundation, under Grant No. PHY-1803047. H.W. would like to thank the Royal Thai Government for financial support of his Ph.D. studies, of which this work was a part.

AUTHOR DECLARATIONS

Conflict of Interest

The authors have no conflicts to disclose.

Author Contributions

W. Hongtrakul: Conceptualization (equal); Investigation (lead); Methodology (equal); Writing – original draft (lead). **C. A. Ordonez**: Conceptualization (equal); Investigation (supporting); Writing – review & editing (equal). **D. L. Weathers**: Conceptualization (equal); Investigation (supporting); Methodology (equal); Supervision (lead); Writing – review & editing (equal).

DATA AVAILABILITY

The data that support the findings of this study are available within the article or from the corresponding author upon reasonable request.

REFERENCES

[1]C. Amole, M. D. Ashkezari, M. Baquero-Ruiz, W. Bertsche, E. Butler, A. Capra, C. L. Cesar, M. Charlton, A. Deller, S. Eriksson, J. Fajans, T. Friesen, M. C. Fujiwara, D. R. Gill, A. Gutierrez, J. S. Hangst, W. N. Hardy, M. E. Hayden, C. A. Isaac, S. Jonsell, L. Kurchaninov, A. Little, N. Madsen, J. T. K. McKenna, S. Menary, S. C. Napoli, K. Olchanski, A. Olin, P. Pusa, C. Ø. Rasmussen, F. Robicheaux, E. Sarid, C. R. Shields, D. M. Silveira, C. So, S. Stracka, R. I. Thompson, D. P. van der Werf, J. S. Wurtele, A. Zhmoginov, L. Friedland, and ALPHA Collaboration, "Experimental and computational study of the injection of antiprotons into a positron plasma for antihydrogen production," Phys. Plasmas **20**, 043510 (2013).

[2]C. A. Ordonez and D. L. Weathers, "Two-species mixing in a nested Penning trap for antihydrogen trapping," Phys. Plasmas **15**, 083504 (2008).

[3]J. Fajans and C. M. Surko, "Plasma and trap-based techniques for science with antimatter," Phys. Plasmas **27**, 030601 (2020).

[4]F. Currell and G. Fussmann, "Physics of electron beam ion traps and sources," IEEE Trans. Plasma Sci. **33**, 1763 (2005).

[5]Y. Gu and G. H. Miley, "Experimental study of potential structure in a spherical IEC fusion device," IEEE Trans. Plasma Sci. **28**, 331 (2000).

[6]J. Hedditch, R. Bowden-Reid, and J. Khachan, "Fusion energy in an inertial electrostatic confinement device using a magnetically shielded grid," Phys. Plasmas **22**, 102705 (2015).

[7]C. A. Ordonez and D. L. Weathers, "Centrifugal-electrostatic confinement fusion," Phys. Plasmas **30**, 092111 (2023).

[8]M. Maggiore, M. Cavenago, M. Comunian, F. Chirulotto, A. Galatà, M. De Lazzari, A. M. Porcellato, C. Roncolato, S. Stark, A. Caruso, A. Longhitano, F. Cavaliere, G. Maero, B. Paroli, R. Pozzoli, and M. Romé, "Plasma-beam traps and radiofrequency quadrupole beam coolers," Rev. Sci. Instrum. **85**, 02B909 (2014).

[9]T. J. Dolan, "Review article: Magnetic electrostatic plasma confinement," Plasma Phys. Controlled Fusion **36**, 1539–1593 (1994).

[10]V. I. Tereshin, K. N. Stepanov, and E. D. Volkov, and IPP NSC KIPT Team, "Researches on plasma physics and controlled fusion in IPP NSC KIPT," Probl. At. Sci. Technol., Ser.: Plasma Phys. **12**(6), 3–9 (2016).

[11]O. A. Lavrent'ev, V. A. Maslov, S. V. Germanova, M. G. Nozdrachev, and V. P. Oboznyi, "Neutral gas influence on plasma heating and confinement in the multislit electromagnetic trap 'JUPITER 2M,'" Probl. At. Sci. Technol., Ser.: Plasma Phys. **5**(3), 48–50 (2000).

[12]O. A. Lavrent'ev, V. A. Maslov, M. G. Nozdrachov, V. P. Oboznyj, S. A. Golyuk, and N. A. Krutko, "Multislit electromagnetic trap 'JUPITER 2M3,'" Probl. At. Sci. Technol., Ser.: Plasma Phys. **13**(1), 27–29 (2007).

[13]C. A. Ordonez, "Drifting plasma confinement with a spatially periodic field," IEEE Trans. Plasma Sci. **38**, 388–392 (2010).

[14]C. A. Ordonez, "Charged particle reflection from an artificially structured boundary that produces a spatially periodic magnetostatic field," J. Appl. Phys. **106**, 024905 (2009).

[15]J. L. Pacheco, C. A. Ordonez, and D. L. Weathers, "Artificially structured boundary for a high purity ion trap or ion source," Nucl. Instrum. Methods Phys. Res., Sect. B **332**, 312–316 (2014).

[16]J. L. Pacheco, C. A. Ordonez, and D. L. Weathers, "Space-charge-based electrostatic plasma confinement involving relaxed plasma species," Phys. Plasmas **19**, 102510 (2012).

[17]R. M. Hedlof and C. A. Ordonez, "Artificially structured boundary plasma trap," Phys. Plasmas **26**, 092509 (2019).

[18]A. S. Kiester, C. A. Ordonez, and D. L. Weathers, "Ionized molecular hydrogen build-up and confinement inside the space charge of a continually resupplied electron cloud," IEEE Trans. Plasma Sci. **50**, 210–221 (2022).

[19]J. P. Verboncoeur, A. B. Langdon, and N. T. Gladd, "An object-oriented electromagnetic PIC code," Comput. Phys. Commun. **87**, 199–211 (1995).

[20]V. Vahedi and M. Surendra, "A Monte Carlo collision model for the particle-in-cell method: Applications to argon and oxygen discharges," Comput. Phys. Commun. **87**, 179–198 (1995).

[21]O. Chubar, P. Elleaume, and J. Chavanne, "A three-dimensional magnetostatics computer code for insertion devices," J. Synchrotron Radiat. **5**, 481 (1998).

[22]K. Gomberoff, J. Fajans, A. Friedman, D. Grote, J.-L. Vay, and J. S. Wurtele, "Simulations of plasma confinement in an antihydrogen trap," Phys. Plasmas **14**, 102111 (2007).

[23]K. Gomberoff, J. Fajans, J. Wurtele, A. Friedman, D. P. Grote, R. H. Cohen, and J.-L. Vay, "Simulation studies of non-neutral plasma equilibria in an electrostatic trap with a magnetic mirror," Phys. Plasmas **14**, 052107 (2007).

[24]K. Gomberoff, J. Wurtele, A. Friedman, D. Grote, and J.-L. Vay, "A method for obtaining three-dimensional computational equilibrium of non-neutral plasmas using WARP," J. Comput. Phys. **225**, 1736–1752 (2007).